applied sciences

MDPI

Article

Development of an Eddy Current Test Configuration for Welded Carbon Steel Pipes under the Change in Physical Properties

Azouaou Berkache [1], Jinyi Lee [1,2,3,*], Dabin Wang [1] and Duck-Gun Park [4]

[1] IT-Based Real-Time NDT Center, Chosun University, Gwangju 61452, Korea; azouaoubrk@chosun.ar.kr (A.B.); anydabin@chosun.kr (D.W.)
[2] Department of Electronics Engineering, Chosun University, Gwangju 61452, Korea
[3] Interdisciplinary Program in IT-Bio Convergence System, Chosun University, Gwangju 61452, Korea
[4] Department of Material Safety, Korea Atomic Energy Research Institute & AIPIT Inc., Daejeon 34057, Korea; dgpark@kaeri.re.kr
* Correspondence: jinyilee@chosun.ac.kr

Abstract: Carbon steel pipe is used in various industries, including nuclear power plants. Due to the daily cyclic operation of the pipe over time, environmental influences, and extreme working conditions, the probability of developing small fine cracks in the welded areas of the pipes increases. For that reason, it requires earlier assessment, and providing adequate inspection and evaluation of the weld area of the pipes used in such an installation is crucial to increase the safety level. In this paper, two different probe configurations were used to assess the integrity of the girth weld of the SA106 carbon steel pipe welded by gas tungsten arc welding. The conventional eddy current probe was initially used, but as it had some limitations, a new probe configuration was proposed to overcome these constraints. Numerical simulations using the finite element method were performed, based on the real measurement of the physical properties of the specimen, to complement the experimental data. In addition, the experimental results were successfully reproduced by the simulations. Simulation and experimental results show that the proposed probe configuration allows adequate inspection.

Keywords: carbon steel pipe; finite element method; short fine cracks; weld area; eddy current testing; change in the physical properties

Citation: Berkache, A.; Lee, J.; Wang, D.; Park, D.-G. Development of an Eddy Current Test Configuration for Welded Carbon Steel Pipes under the Change in Physical Properties. *Appl. Sci.* **2022**, *12*, 93. https://doi.org/10.3390/app12010093

Academic Editor: Jean-Pierre Bergmann

Received: 24 November 2021
Accepted: 21 December 2021
Published: 22 December 2021

1. Introduction

Carbon steels are common in a wide variety of applications owing to their low cost and excellent mechanical properties. These range from marine applications, buildings and bridges, domestic appliances, the automotive industry, the oil and gas industry, and especially to power plants, among them nuclear power plants, which have many piping systems carrying fluids and gases [1–5].

Welding and joining processes such as arc welding, laser welding, and friction stir welding are used to assemble and join the main parts of such structures [6–8]. Welding has the advantage of having relatively few restrictions on the thickness and shape of the target material, reducing the weight of the equipment, and solving the problems of size limits, as parts produced in small sizes can be combined with the welding process to become larger parts [9–11].

However, despite the fact that welding is considered one of the most important manufacturing processes, during this process the weld area undergoes compression and expansion caused by rapid temperature changes and mechanical stresses, residual stresses that lead to a reduction in structural integrity and which affect the mechanics of the joint. Among the most important types of failures, which occur frequently, are fatigue and stress corrosion cracking (SCC), which may lead to cracking in service, with consequences such as leakage and even structural failure. In particular, the possibility of such failures is greatly

increased during long-term operation in high-temperature, high-pressure, and corrosive environments [12–17].

Therefore, to secure the safety of the installations (plants), the integrity of the pipes and weld joints should be assured. To achieve this, non-destructive testing (NDT) is performed on the welds to be inspected during the planned preventive maintenance period to confirm the integrity evaluation of pipe weld inspections according to the ASME code requirements. During this period, the correct welding parameters/procedures should be selected to prevent the formation of defects of various types [18–21].

Numerous non-destructive testing (NDT) methods, namely eddy current testing (ECT), radiography testing, ultrasonic testing, magnetic particle testing, penetrant testing, and so on, can be applied as industrial methods to investigate the integrity of welds in assembled pipes [22–25]. The ECT technique has many advantages such as high detection sensitivity, no coupling agent, no contact between the test specimen and the sensor, and the ability to detect parts in-line. In addition, the technique is appropriate for a variety of conductive materials, either ferromagnetic or non-ferromagnetic [26–28]. Certain factors affect the response of an eddy current probe, namely the frequency, magnetic permeability, and conductivity of the specimen. The electrical conductivity and magnetic permeability of the specimen depend on the microstructure of the specimen. They are related to the skin depth, given by the expression (1) [29,30]:

$$\delta_s = \sqrt{\frac{2}{\omega\sigma\mu}} \tag{1}$$

where ω, σ, and μ are the angular frequency, the conductivity, and the permeability, respectively. In addition, the ECT is strongly affected by the lift-off, which can be defined as the separating distance between the surface of the excitation coil and the surface of the conducting material.

A number of research studies have been performed to enhance defect characterization with regard to the reduction of the lift-off effect, new design and optimization of probes, and feature extraction [31,32]. Our focus is on research studies on crack detection in carbon steel specimens using the finite element method (FEM). Xu et al. [33] proposed a new rotating field EC probe for defect detection on carbon steel using finite element analysis and found that the excitation strategy gives the designed probe advantages for arbitrary orientation defect detection. In a similar way, Huang et al. [34] designed a new type of eddy current probe to detect defects on the weld of carbon steel using finite element simulation to suppress the effect of the weld surface on the lift-off effect during the detection process, and to maintain a high sensitivity when detecting the weld. Zhang et al. [35] investigated the behavior of the eddy current testing signal to ferromagnetic carbon steel and non-ferromagnetic stainless steel by using the finite element method, and the results reveal that the magnetic field detected for a ferromagnetic material is the superposition of the magnetic field induced by the eddy current and the magnetic flux leakage.

In this paper, the position and size of the studied cracks are assumed to be the most important. They are considered to be short thin external cracks and are more dangerous than internal cracks from a practical point of view [36].

However, despite the importance of the quality control of the integrity of the sample, especially the joints, there are no considerations of the real physical characteristics in the works cited above. Residual stresses and heat treatment during the welding process are the main factors causing a change in the same batch specimen, resulting in the microstructural differences which determine the mechanical and physical properties. For the accurate evaluation of the girth weld in assembled carbon steel pipes, the simulation investigations were carried out by measuring the real physical parameters (electrical conductivity and the relative permeability) of the specimen in the target areas: raw, heat affected zone (HAZ), and weld area. The conventional vertical probe is used; then, as an alternative to this probe, as the signal is noisy, a horizontal probe is proposed for a better examination. In

addition, the simulation of the cracks in the circumference weld by finite element analysis (FEA) is performed, based on the experimental considerations, to take into account the effect of temperature on the physical properties in the numerical model used. The findings of the research were examined by comparing them with the experimental measurements. In addition, they highlight that the suggested probe configuration allows for better examination.

2. Materials and Methods

Experimental work was performed to verify the simulation findings, and the configuration of the experiment is illustrated in Figure 1. The same experiment was carried out with two coil configurations (positions), the first using a vertical probe and the second a horizontal probe. In the first case, ECT equipment was utilized. It is an Olympias Nortek 500 eddy current fault detector, which monitors the power supply and frequency. The signal obtained from this system is passed to a laptop through an analog-to-digital converter. Moreover, in the second experiment, a power supply was used to generate the input power and frequency. The SA106 pipe was placed on a rotating stage platform and the ECT probe and coil were fixed parallel to the pipe to scan the different regions of the pipe, from x = 0 to x = 40 mm with a constant scanning step of 1 mm. The position of the probe can be adjusted to minimize the lift-off difference that may be caused by the banding surface of the pipe and provide the same test conditions for each scan. The heat-affected zone length is deemed to be 12.7 mm (1/2 inch), in conformity with the KEPIC MI technical standard [18]. The experimental investigations were conducted by an ASNT Level II qualified examiner by complying to the ISO 7912 instructions [37].

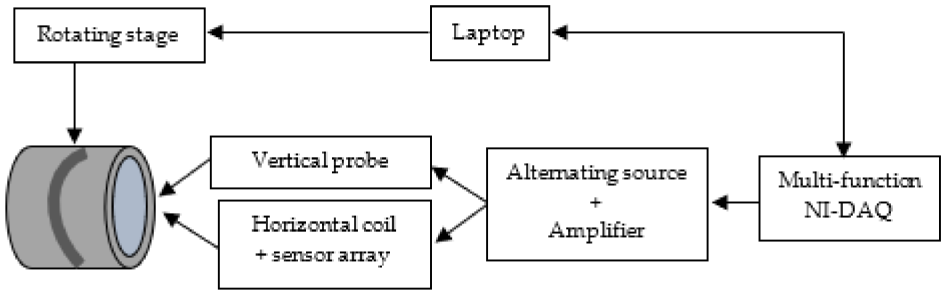

(**a**)

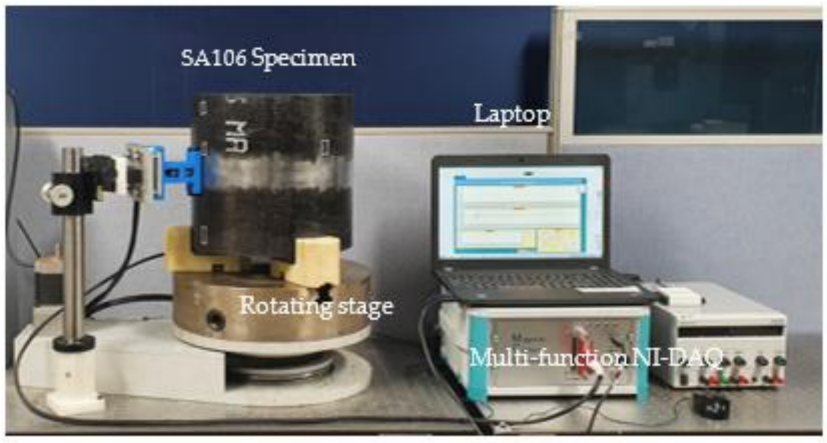

(**b**)

Figure 1. Experimental setup. (**a**) Bloc diagram of ECT equipment and (**b**) inspection setup.

Prefabricated cracks were made by the electrical discharge machining (EDM) process and introduced into the weld area. Their length and width are 5 mm and 0.2 mm with different depths (0.3 mm, 0.5 mm, and 1.0 mm), designated as (C0.3, C0.5, and C1.0),

respectively, as shown in Figure 2. The inner diameter, outer diameter, and height of the conventional vertical probe are 3 mm, 4 mm, and 7.5 mm. The sensor probe shown in Figure 3 has a LIGiS placed under an air core exciting coil [38], as illustrated in Figure 4. The exciting coil is made of 0.2 mm diameter copper wire. The LIGiS has 32 GMR sensor elements arrayed at 0.6 mm intervals to form a sensing length of 19.2 mm. The GMR sensors are oriented at 45° to the array length to prevent their saturation by the magnetic field of the exciting coil. The sizes of the horizontal probe are listed in the same figure.

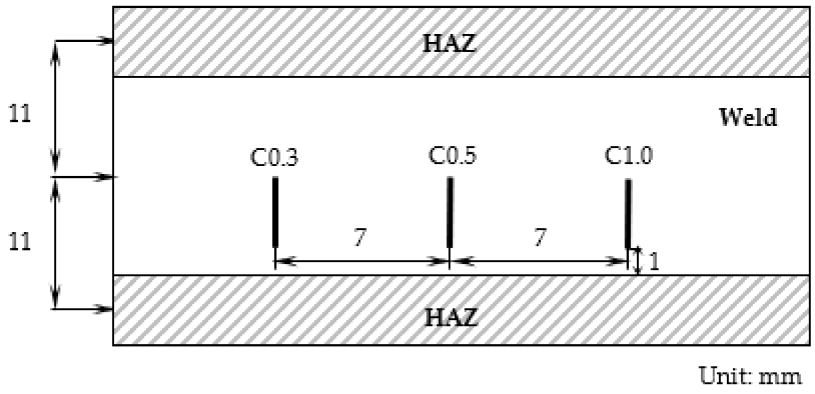

Figure 2. Specimen with artificial narrow cracks.

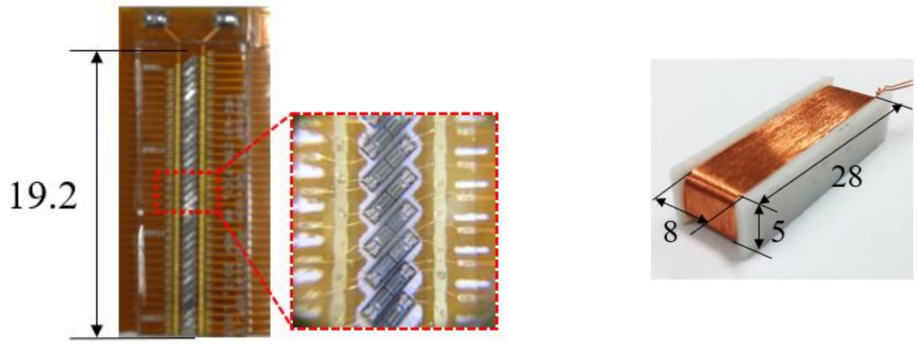

Figure 3. (**a**) Sensor array and (**b**) exciting coil (unit: mm).

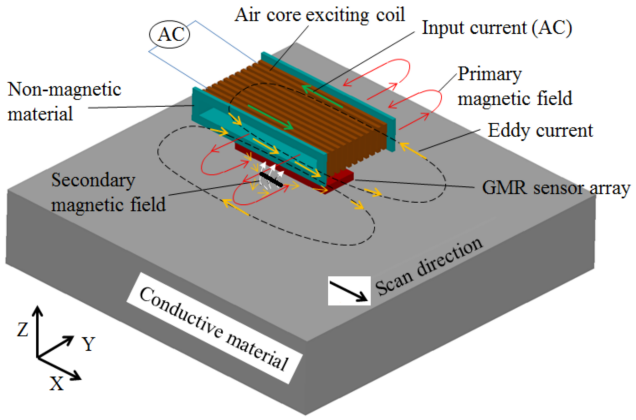

Figure 4. Scan configuration.

According to the Faraday–Lenz law, the electromagnetic force V_{emf} is defined by the following equation:

$$V_{emf} = -N\frac{d\varnothing}{dt} = -N\int_s \frac{\partial \vec{B}}{dt}\vec{ds} \quad (2)$$

where N, $\frac{\partial \vec{B}}{dt}$, and s are the numbers of turns of the coil, frequency of excitation, and area of the coil probe, respectively. To achieve a good S/N ratio, a large, high frequency probe with many turns is required. A high excitation frequency is limited in ferromagnetic materials such as carbon steel due to the skin depth given in Equation (1). In addition, the large probe is limited by the spatial resolution of the sensor array. Furthermore, the electromagnetic interference of each sensor and the coverage performance are affected in the vertical probe array. To reduce the electromagnetic interference and improve the coverage performance, a single large excitation coil is used. As well, to improve the spatial resolution, the density of the induced magnetic flux density around the crack is detected using semiconductor based on GMR sensors. Finally, the longitudinal direction of the induced current on the specimen must be parallel to the weld wave (marks) in order to reduce noise due to weld marks and weld beads. The excitation coil has a shape of shallow perpendicular, the direction of the air core is parallel to the weld line, the vertical direction of the GMR sensor array is parallel to the weld line, i.e., parallel to the coil length direction, the GMR sensor arrays are located beside the coil and the sample, each GMR sensor is gradient with the array line, and the scan direction follows the weld line. The geometrical and physical characteristics of the test specimen are listed in Table 1. In the heat-affected zone, the electrical conductivity is gradiently decreasing from the weld to the base material $\sigma_1 = 28 \sim 18$ μΩ/cm and the relative permeability is gradiently increasing also from the weld to the base material $\mu_1 = 201 \sim 260$.

Table 1. Geometric and physical parameters of the test pipe.

Geometric Parameters		Physical Parameters	
Inner diameter	311 mm	Specimen conductivity	18 μΩ/cm
Outer diameter	320 mm	Weld conductivity	28 μΩ/cm
Thickness	9 mm	Specimen permeability	260
Weld width	12 mm	Weld permeability	201

For the measurement of the electrical conductivity and the relative permeability of the welded carbon steel pipe, a micro-ohmmeter and a DC B-H loop tracer were used, as illustrated in Figure 5. The measurement condition was 23 °C (room temperature) and the measurement was performed by the 4-point method.

(**a**) (**b**)

Figure 5. Conductivity and permeability measuring equipment: (**a**) Conductivity meter; (**b**) DC B-H loop tracer.

3. Governing Equations

3.1. Magnetic Field FEM Formulation

The electromagnetic field model is obtained with the consideration of assumptions that the conduction current is assumed to be dominant and therefore the displacement current is neglected. It is based on Maxwell's equations and on the concept of magnetic vector potential (MVP) in a quasi-stationary state, defined as follows [39–41]:

$$\vec{\nabla} \times \left(\frac{1}{\mu} \left(\vec{\nabla} \times \vec{A} \right) \right) + j\omega\sigma\vec{A} = \vec{J}_S \tag{3}$$

$\vec{A}$—the magnetic vector potential, $\vec{J}_S$—the source current density, μ—the magnetic permeability, σ—the electrical conductivity, and ω—the angular frequency.

In the heat-affected zone, the relative permeability and the electrical conductivity are noted with indices (1) and given as $\mu_1 = [\mu_a \ldots\ldots\ldots \mu_{T_{HAZ}}]$ and $\sigma_1 = [\sigma_a \ldots\ldots\ldots \sigma_{T_{HAZ}}]$. T_{HAZ} denotes the total number of triangular elements obtained from the finite element meshing in the heat-affected zone. After the mesh creation step, the electrical conductivity and the relative permeability are distributed in accordance with the number of elements contained in the heat-affected zone area, exploiting the generation of pseudo-random numbers to reproduce the distribution of these physical properties on the basis of the experimental measurement. Then, the obtained algorithms are combined with the finite element code [25].

Applying the vectors weighting functions α_i, the weighted Galerkin residual equation is obtained from Equation (1), as set out below:

$$\iint_{\Omega} \alpha_i \left(\vec{\nabla} \times \left(\frac{1}{\mu} \left(\vec{\nabla} \times \vec{A} \right) \right) + j\omega\sigma\vec{A} \right) d\Omega = \iint_{\Omega} \alpha_i \, \vec{J}_S \, d\Omega \tag{4}$$

After applying discretization and assembly, the following algebraic system is derived:

$$([K] + j\omega[M])[A] = [F] \tag{5}$$

$$K_{ij} = \iint_{\Omega} \frac{1}{\mu} \vec{\nabla}\alpha_i \, \vec{\nabla}\alpha_j \, d\Omega \tag{6}$$

$$M_{ij} = \iint_{\Omega} \sigma \, \alpha_i \, \alpha_j \, d\Omega \tag{7}$$

$$F_i = \iint_{\Omega} \alpha_i \, \vec{J}_S \, d\Omega \tag{8}$$

where: $[K]$, $[M]$, $[A]$, and $[F]$ are the stiffness matrix, dynamic matrix, unknowns vector, and source vector, respectively.

3.2. Impedance Computation

Eddy current testing is one of the techniques for inspecting the subsurface and surface layers of metals, which is important for various industrial applications. During the electromagnetic interaction between the probe and the metal specimen, the properties of the specimen and the presence of material deposits, corrosion, and cracks influence the probe's information, resulting in changes in the impedance of the probe. In this context, the impedance is expressed as a function of the magnetic vector potential (MVP), given as [25,42]:

$$Re(Z) = -\frac{N^2}{J \, S^2} \omega \iint_{S} 2\pi r \, Im(A) \, ds \tag{9}$$

$$Im(Z) = -\frac{N^2}{J\,S^2}\omega \iint_S 2\pi r\; Re(A)\; ds \tag{10}$$

where: N, S, and r are the coils number, surface of inductor coil, and inductor radius.

4. Results and Discussion

The specific objective of this work is to evaluate and improve the ability to detect narrow cracks in carbon steel weld joints with the eddy current testing technique. So, it is critical to investigate, identify, and control the formation and growth of such cracks to reduce the threat of unexpected failure. For this purpose, very accurate solutions and measurement data are required. It is obvious that numerical analysis plays a crucial role in the solution of the ECT probe. This is why the finite element method is used.

The radius of the tube of the carbon steel specimen under investigation is considerably bigger than the size of the probes and the surface area is relatively larger than the probes, so the wall of the tube can be considered as a plate, and the problem is simplified and can be modeled as two-dimensional geometry [25,43,44]. On the other hand, the configuration shown in Figure 6a (3D configuration) is streamlined, as shown in Figure 6c (2D configuration), which is representative of the specimen, the single coil, and the narrow crack. The corresponding schematic structure of the device is depicted in Figure 7, in which the various parts of the device are listed directly.

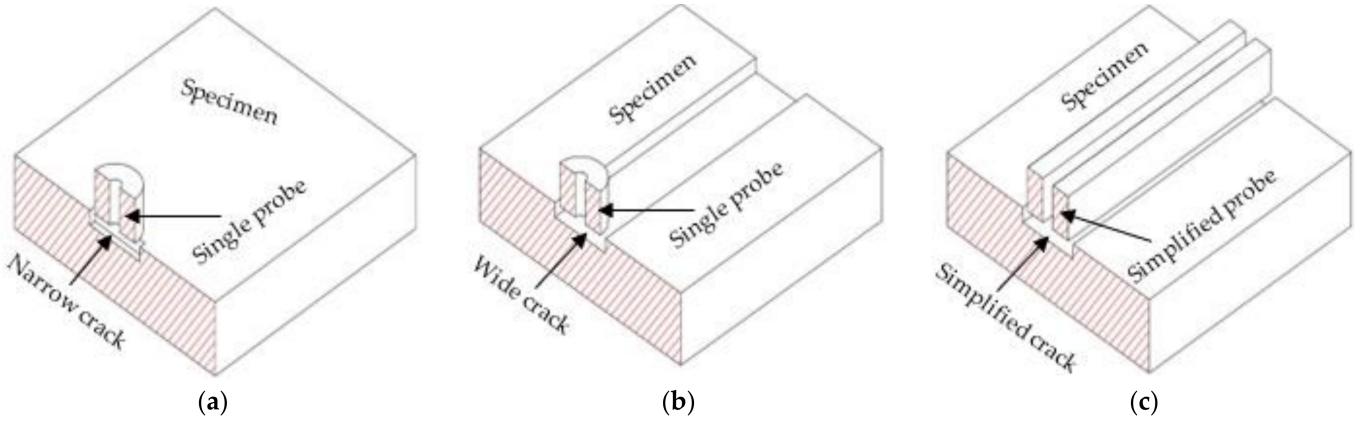

Figure 6. Same section views with (**a**) 3D configuration, (**b**) 3D configuration with long defect, and (**c**) amended 3D configuration to a 2D configuration.

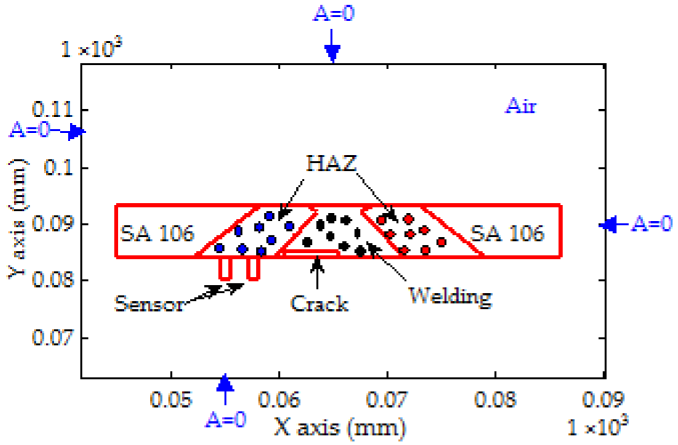

Figure 7. Solving domain and boundary conditions.

In Figure 8a, the entire geometry is then covered by a finite element mesh, consisting of triangular elements obtained by a mesh generator based on the MATLAB Partial Differential

Equation Toolbox. This toolbox enables the generation of a mesh using the Delaunay triangulation algorithm. The selection of an appropriate mesh density for the reliability analysis is important, especially around the crack region, to achieve reliable results. Due to the symmetrical distribution of these properties, the distribution represented covers a path of 20 mm from the center length of the inspected part to the last inspected point, as illustrated in Figure 9.

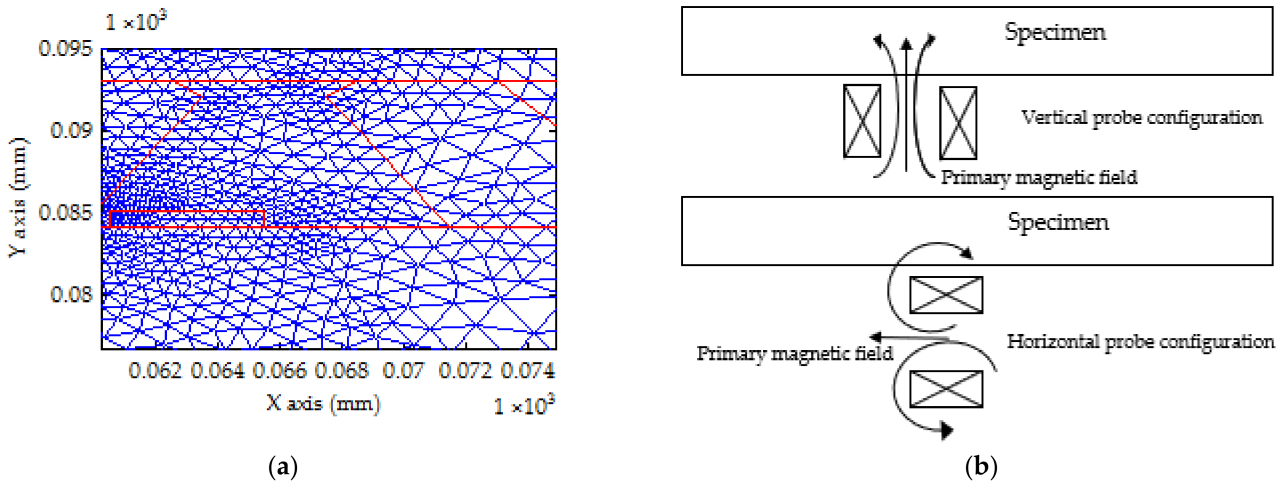

(**a**) (**b**)

Figure 8. (**a**) Finite element mesh; (**b**) Excitation probe configurations.

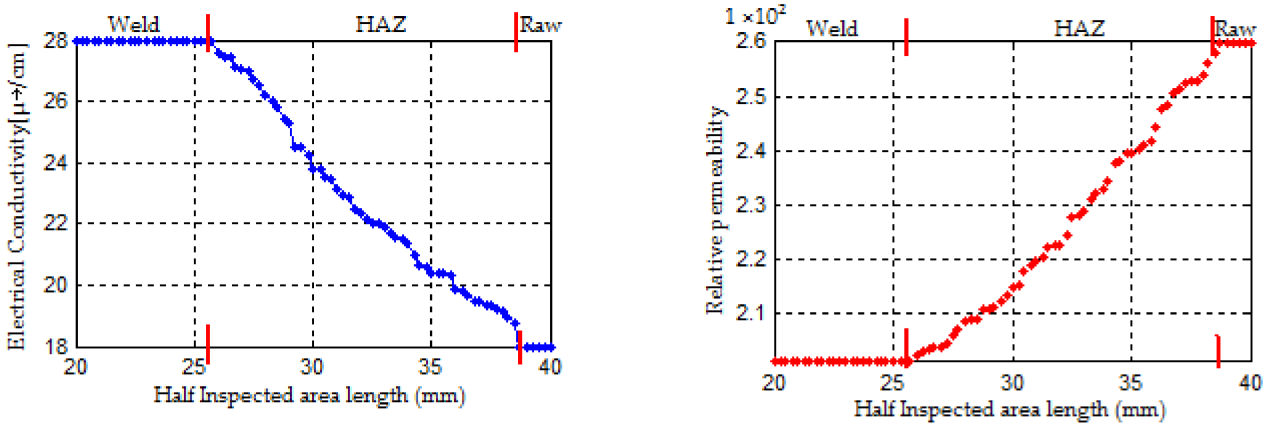

(**a**) (**b**)

Figure 9. Physical properties distributions: (**a**) Electrical conductivity distribution; (**b**) Relative permeability distribution.

Considering the need for detecting the deeper crack to achieve larger skin depth and to control the surface of inspected pipe, a compromise is made by considering the operating frequency, detection, and optimum frequency, with a lift-off of 0.1 mm. The distance and scan pitch simulated were identical to the experimental parameters. A fixed scan distance of 40 mm was chosen so that the cracks are located at the half-center of the weld zone along the scan trajectory.

The impedance signal amplitudes obtained for all the used frequencies are normalized and plotted versus the probe displacement. For each crack depth, the corresponding impedance signal amplitude is normalized by the impedance signal amplitude of the 1 mm crack depth. The normalized impedance was computed by $Delta\ Z(\%) = (Z - Z_0)/(Z - Z_{1.0})_{max}$, where Z_0, Z, and $Z_{1.0}$ are the impedances of the raw material without crack, the impedance from the HAZ and the weld with the crack, and the impedance

from the weld of the 1 mm crack depth, respectively. To give an overview of the influence of noise and to facilitate the interpretation of the results presented below, the quantity $(Z - Z_0)$ is given here. The value of the noise is almost the same for both configurations $0.01 \sim 0.03$. However, the quantity $(Z - Z_0)$ is different from each configuration. For instance, with 40 kHz, using the vertical configuration, this quantity is equal to 0.06, 0.075, and 0.11 Ω according to the cracks (C0.3, C0.5, and C1.0), respectively, while this same quantity is more important in terms of value with the horizontal configuration, as it corresponds to 0.1, 0.16, and 0.21 Ω, always respecting the designation of the cracks.

The comparison between the simulation and the experimental data is undertaken for the three depths (0.3 mm, 0.5 mm, and 1 mm), and the outcomes of the crack depth relationships, indicating that deeper cracks have larger delta Z values, are presented in Figures 10–16.

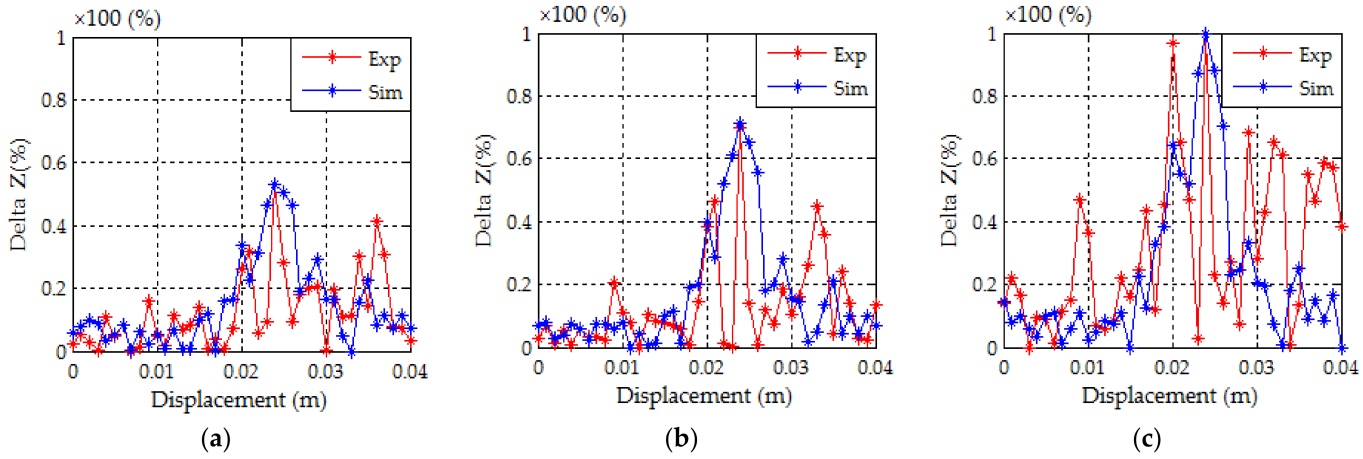

Figure 10. Impedance variation in (%) at 10 kHz with (**a**) depth = 0.3 mm, (**b**) depth = 0.5 mm, and (**c**) depth = 1 mm.

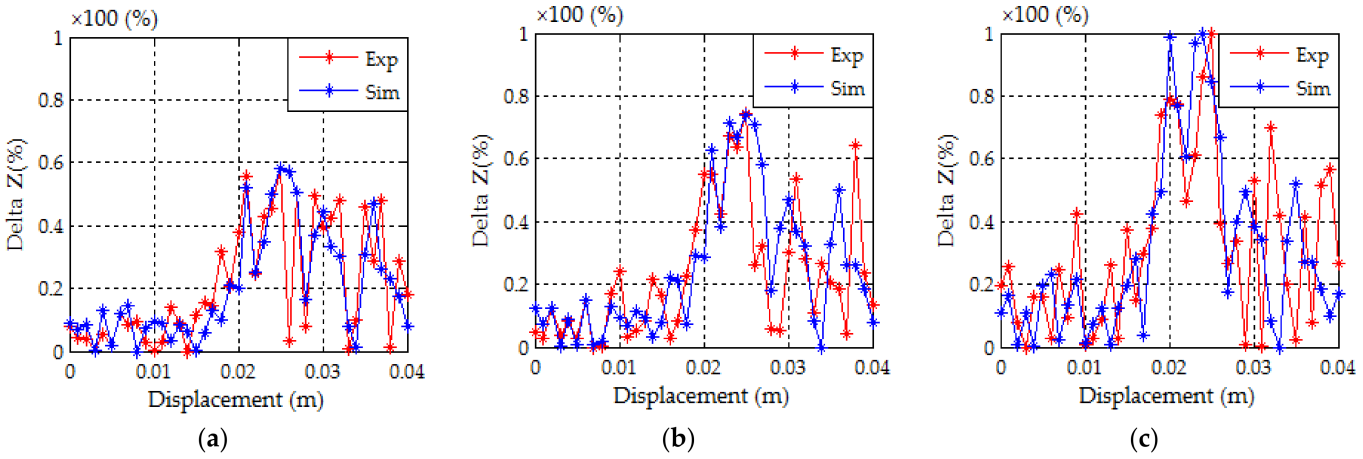

Figure 11. Impedance variation in (%) at 20 kHz with (**a**) depth = 0.3 mm, (**b**) depth = 0.5 mm, and (**c**) depth = 1 mm.

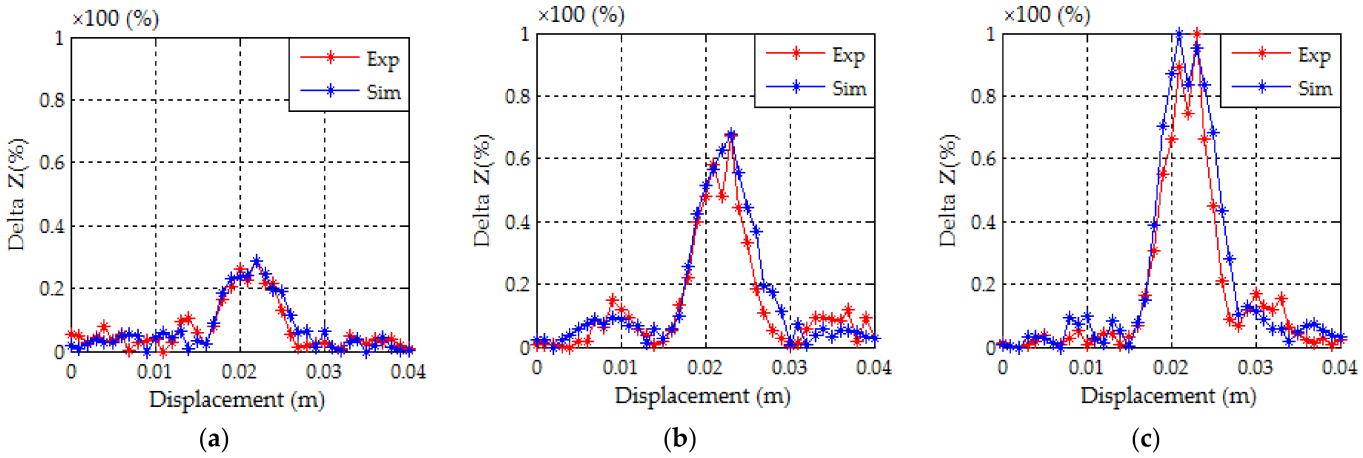

Figure 12. Impedance variation in (%) at 40 kHz with (**a**) depth = 0.3 mm, (**b**) depth = 0.5 mm, and (**c**) depth = 1 mm.

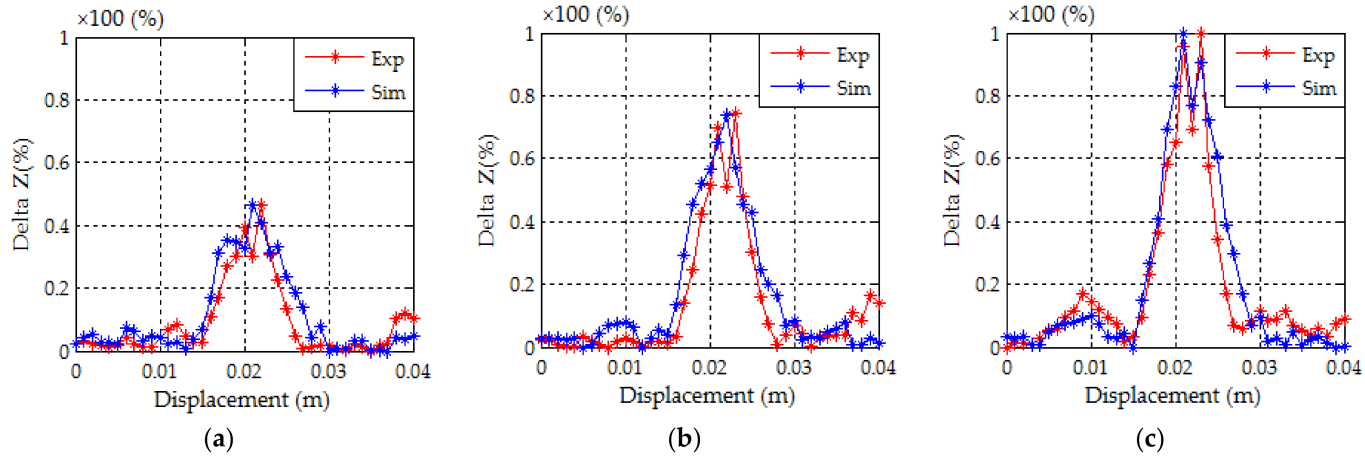

Figure 13. Impedance variation in (%) at 10 kHz with (**a**) depth = 0.3 mm, (**b**) depth = 0.5 mm, and (**c**) depth = 1 mm.

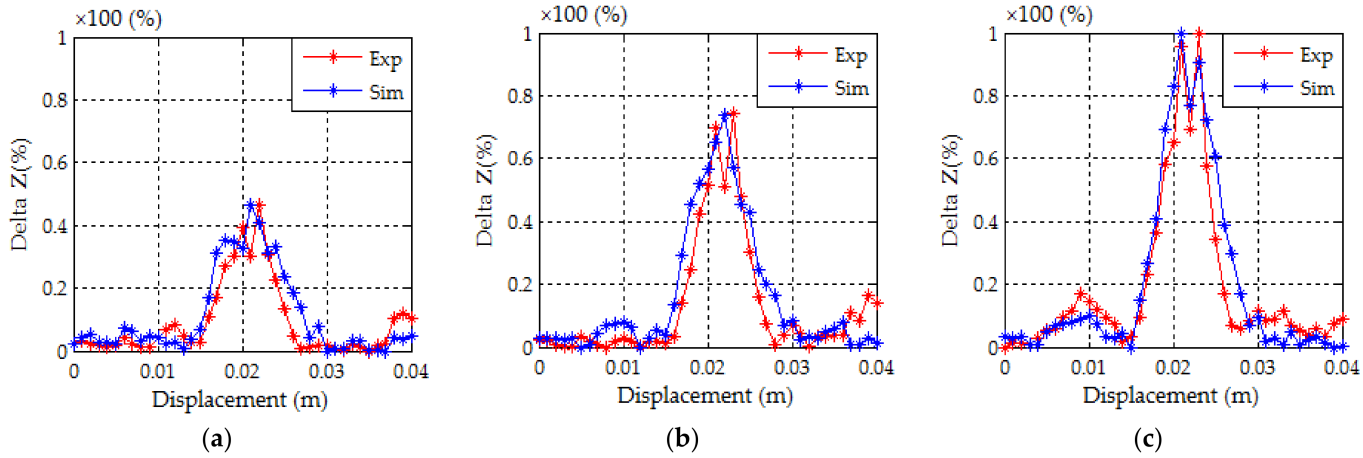

Figure 14. Impedance variation in (%) at 20 kHz with (**a**) depth = 0.3 mm, (**b**) depth = 0.5 mm, and (**c**) depth = 1 mm.

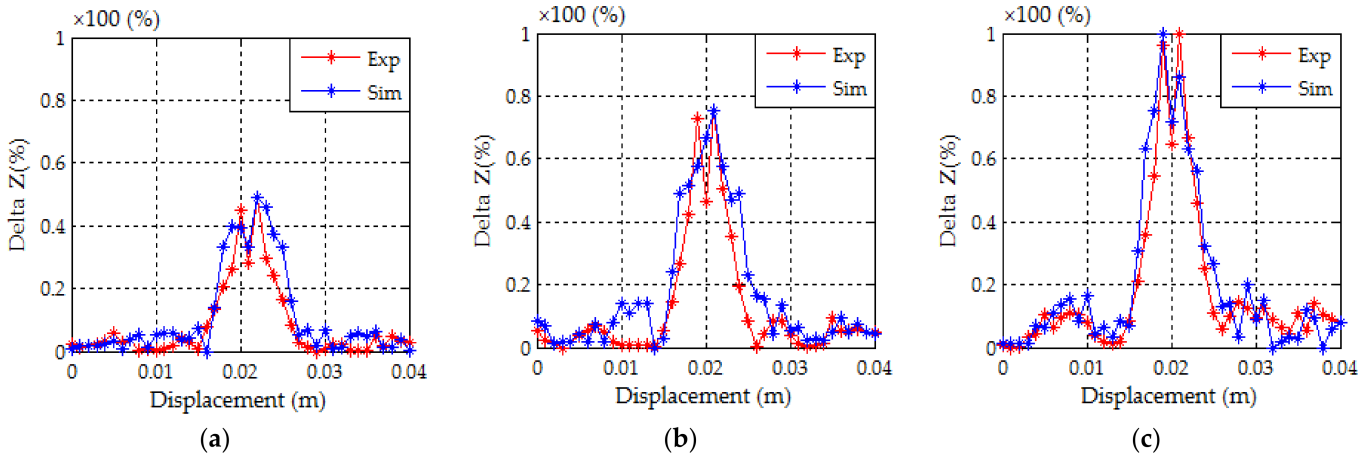

Figure 15. Impedance variation in (%) at 40 kHz with (**a**) depth = 0.3 mm, (**b**) depth = 0.5 mm, and (**c**) depth = 1 mm.

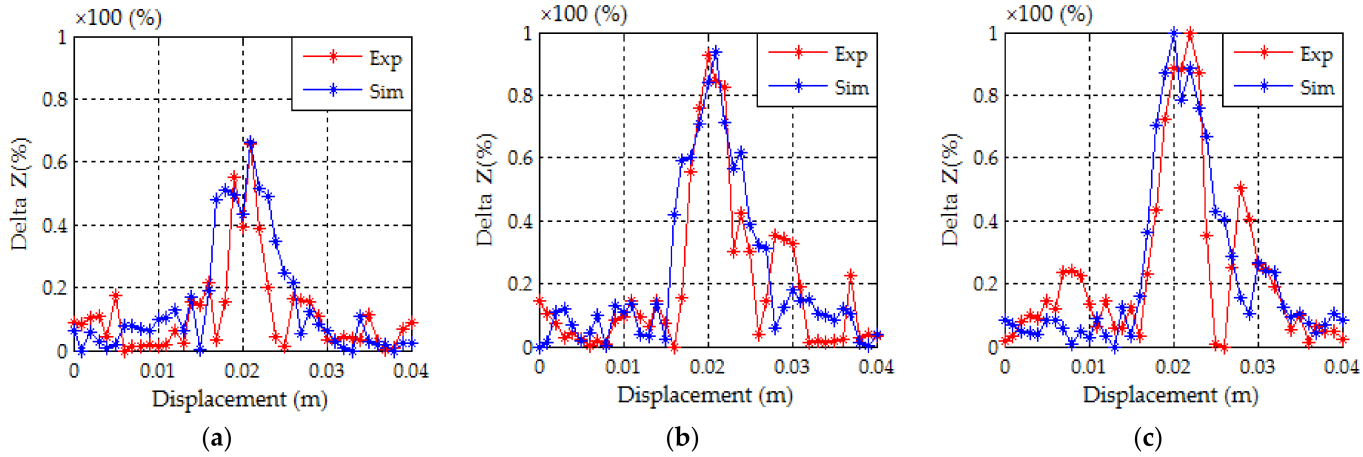

Figure 16. Impedance variation in (%) at 80 kHz with (**a**) depth = 0.3 mm, (**b**) depth = 0.5 mm, and (**c**) depth = 1 mm.

As shown in Figures 10–12, the output signals from the ECT measurement experiments are noised. However, the narrow cracks being visible and the noise appearing in the signal would not be considered sufficiently continuous to be called cracks. In Figure 12a, there are noise signals that would be confused with cracks. So, it is not easy to judge the existence or absence of narrow cracks from the signal's behavior. This is probably due to the uneven and banding shape surface of the carbon steel, the variation of the lift-off of a probe, and the presence of structures on the pipe surface. In the simulation, it is probably due to the change in physical properties. From the same Figures 10–12, the signal is small and because of that the noise appears to be high.

To overcome this limitation and the lack of precision of the conventional probe given in Figure 8b, detecting and finding defects in weld joints while reducing the signal noise usually involves obtaining information through proper inspection, for which greater accuracy is required. To achieve this, a horizontal probe design (with an exciting coil used as an emitter and a GMR as receiver, both for simulation and experiment) may potentially lead to better detection and avoid such noises as proposed.

In order to fully assess the behavior of the probe's output signals as it scans the pipe's different zones, and to propose a suitable configuration of the probe, the use of the finite element analysis offers significant advantages in addressing this issue. The frequency is a critical factor in eddy current testing. It relates to the skin depth and the amplitude of the probe signal. This parameter must be selected appropriately by the experimenter.

The experimental distribution of the SA106 specimen properties is reproduced by means of the Monte Carlo method based on PRNG in order to conceive a numerical model that reflects the real model of the studied problem, which is important to evaluate the impact of the heat treatment on these properties in the presence of cracks as it allows a proper evaluation and comparison of the response derived with the experimental ones.

The distribution of electrical conductivity and magnetic permeability are almost symmetrical with respect to the symmetry position of the device (x = 20). The carbon steel was massive, and the impedance was calculated from the magnetic vector potential, and it also remains symmetric regarding the symmetry position of the device. The behavior of the impedance signal increases gradually to attain a maximum amplitude and afterwards decreases until the last displacement of the probe. Fluctuations at the peak of the Delta impedance amplitude appear, indicating a change in the physical milieu, i.e., a change in physical properties (the crack and weld). This is explainable, as it indicates the existence of narrow cracks in the weld area.

In Figures 10–12, which correspond to the vertical probe configuration, the ECT signals are significantly affected by the relative permeability and electrical conductivity changing gradiently randomly in the HAZ due to the heat treatment. This change then impacts the coupling of the probe to the carbon steel specimen, leading to the occurrence of noises; therefore, the results are not easy to work with.

The results presented in Figures 13–16 clearly show the superiority of the horizontal probe over the vertical probe configuration regarding the apparition of the noises. These noises generated can lead to the misinterpretation of the signals as flaws. The horizontal probe configuration was very efficient with regard to the detection performance of these types of cracks, as it does not generate such noises. Moreover, these results show that the correspondence between the simulation and the experimental results is quite acceptable, while considering various types of influencing factors, including the non-uniform physical properties of the sample, the assumptions made in the 2D simulation while the experiment is in 3D, the probe calibration and the measurement errors caused by the analogue electronic devices involved in the experiment, the variation of the lift-off distance leading in weaker coupling between the probe's electromagnetic field and the specimen, and the machining of cracks. A finite element modeling simulation was used to measure the accuracy detection of the horizontal probe. The comparison of the experimental and simulation data proved the accuracy of the proposed probe.

5. Conclusions

A conventional eddy current probe has been used for the evaluation of narrow cracks in a metal specimen. However, the obtained outcome with this probe reveals that the data are noised and can cause confusion between the cracks and the noises, and thus lead to the misinterpretation of the signal in the weld of the carbon steel pipe. For this purpose, new probe configuration was proposed, and from the results, it has a good reliability for detecting the narrow cracks and offers a suitable NDT method. The implemented model is validated by a comparison showing a satisfactory agreement with the experimental results obtained.

The results have shown that the main factor causing differences in the eddy current output signal is the change in physical properties.

The horizontal probe can be realized on the basis of the following concepts:

- The excitation coil has a shape of shallow perpendicular.
- The direction of the air core is parallel to the weld line.
- The vertical direction of the GMR sensor array is parallel to the weld line, i.e., parallel to the coil length direction.
- The GMR sensor arrays are located beside the coil and the sample.
- Each GMR sensor is gradient with the array line.
- The scan direction follows the weld line.

Cracks are identifiable with both probe configurations:

- The conventional probe configuration enables the identification of cracks, although the data are noisy. The signal is small, so the noise appears large.
- The proposed horizontal probe configuration offers good convergence performance and spatial resolution. The signal is large, so the data appears clearly.

Author Contributions: Conceptualization, J.L. and A.B.; methodology, J.L., A.B. and D.W.; software, A.B.; validation, A.B. and J.L.; formal analysis, A.B.; investigation, J.L. and A.B.; resources, J.L., D.-G.P. and D.W.; data curation, J.L., A.B. and D.W.; writing—original draft preparation, A.B.; writing—review and editing, A.B. and J.L.; visualization, D.-G.P. and J.L.; supervision, J.L.; project administration, J.L.; funding acquisition, J.L. This paper was prepared with the contributions of all authors. All authors have read and agreed to the published version of the manuscript.

Funding: This work was supported by the National Research Foundation of Korea (NRF) grant funded by the Korea government (MSIT) (no. NRF-2019R1A2C2006064).

Institutional Review Board Statement: Not applicable.

Informed Consent Statement: Not applicable.

Data Availability Statement: Not applicable.

Conflicts of Interest: The authors declare no conflict of interest.

Abbreviations

SCC	Stress corrosion cracking
NDT	Non-destructive testing
ECT	Eddy current testing
FEM	Finite element method
HAZ	Heat-affected zone
FEA	Finite element analysis
EDM	Electrical discharge machining
MVP	Magnetic vector potential
ASNT	American Society for Non-Destructive Testing
PRNG	Pseudo-random number generation

References

1. Callister, W.D. *Materials Science and Engineering: An Introduction*, 7th ed.; John Wiley & Sons, Inc.: New York, NY, USA, 2007; ISBN 978-0-471-73696.
2. Jafari, H.; Akbarzade, K.; Danaee, I. Corrosion inhibition of carbon steel immersed in a 1 M HCl solution using benzothiazole derivatives. *Arab. J. Chem.* **2014**, *12*, 1387–1394. [CrossRef]
3. Yan, W.; Chen, W.; Li, J. Quality Control of High Carbon Steel for Steel Wires. *Materials* **2019**, *12*, 846. [CrossRef]
4. Kim, S.-W.; Yun, D.-W.; Chang, S.-J.; Park, D.-U.; Jeon, B.-G. Quantitative Limit State Assessment of a 3-Inch Carbon Steel Pipe Tee in a Nuclear Power Plant Using a Damage Index. *Energies* **2020**, *13*, 6395. [CrossRef]
5. World Steel Association. "World Steel in Figures 2021", Brussels, Belgium. 2021. Available online: https://www.worldsteel.org/publications/infographics.html (accessed on 2 August 2021).
6. Neugebauer, R.; Wiener, T.; Zösch, A. Quality control of resistance spot welding of high strength steels. *Procedia CIRP* **2013**, *12*, 139–144. [CrossRef]
7. Liu, Z.M.; Cui, S.; Luo, Z.; Zhang, C.; Wang, Z.; Zhang, Y. Plasma arc welding: Process variants and its recent developments of sensing, controlling and modeling. *J. Manuf. Process.* **2016**, *23*, 315–327. [CrossRef]
8. Wang, B.; Zhu, X.-M.; Zhang, H.-C.; Zhang, H.-T.; Feng, J.-C. Characteristics of Welding and Arc Pressure in the Plasma–TIG Coupled Arc Welding Process. *Metals* **2018**, *8*, 512. [CrossRef]
9. Crossland, B. *Explosive Welding of Metals and Its Application*; Oxford University Press: New York, NY, USA, 1982; p. 242.
10. Prashanth, K.G.; Damodaram, R.; Scudino, S.; Wang, Z.; Rao, K.P.; Eckert, J. Friction stir welding of Al-12Si, parts produced by selective laser melting. *Mater. Des.* **2014**, *57*, 632–637. [CrossRef]
11. Karayel, E.; Bozkurt, Y. Additive manufacturing method and different welding applications. *J. Mater. Res. Technol.* **2020**, *9*, 11424–11438. [CrossRef]
12. Section XI Task Group for Piping Flaw Evaluation. ASME Code. Evaluation of flaws in austenitic steel piping. *J. Press. Vessel Technol.* **1986**, *108*, 352–366. [CrossRef]

13. Wilkowski, G.M.; Brust, F.; Francini, R.; Ghadiali, N.; Kilinski, T.; Krishnaswamy, P.; Landow, M.; Marschall, C.W.; Rahman, S.; Scott, P. *Short Cracks in Piping and Piping Welds*; Semi Annual Report, October 1990–March 1991; U.S. Department of Energy Office of Scientific and Technical Information: Oak Ridge, TN, USA, 1992; Volume 1.
14. Kuo, T.Y.; Jeng, S.L. Porosity reduction in Nd–YAG laser welding of stainless steel and inconel alloy by using a pulsed wave. *J. Phys. D Appl. Phys.* **2005**, *38*, 722–728. [CrossRef]
15. Huang, T.D.; Conrardy, C.; Dong, P.; Keene, P.; Kvidahl, L.; DeCan, L. Engineering and production technology for lightweight ship structures, Part II: Distortion mitigation technique and implementation. *J. Ship Prod.* **2007**, *23*, 82–93. [CrossRef]
16. Ruminski, A. Failure Analysis of a Low-Temperature Carbon Steel Pipe from a Nuclear Power Station Cooling Water System. *J. Fail. Anal. Prev.* **2015**, *15*, 534–540. [CrossRef]
17. Pankaj, P.; Tiwari, A.; Bhadra, R.; Biswas, P. Experimental investigation on CO_2 laser butt welding of AISI 304 stainless steel and mild steel thin sheets. *Opt. Laser Technol.* **2019**, *119*, 105633. [CrossRef]
18. Korea Electric Association. *MI in Service Inspection of N.P.P.*; Korea Electric Association: Seoul, Korea, 2009; pp. 3–32.
19. American Society of Mechanical Engineers. *ASME Boiler and Pressure Vessel Code*, 2017th ed.; ASME: New York, NY, USA, 2017; Available online: https://pdf4pro.com/view/2017-asme-57c4bb.html (accessed on 28 November 2021).
20. Qian, Z.; Chumbley, S.; Karakulak, T.; Johnson, E. The residual stress relaxation behavior of weldments during cyclic loading. *Metall. Mater. Trans.* **2013**, *44*, 3147–3156. [CrossRef]
21. Naveed, N. Characterisation of short-length scale residual stress variations within an electron beam welded P91 Ferritic–Martensitic steel plate. *Heliyon* **2021**, *7*, 2405–8440. [CrossRef]
22. International Atomic Energy Agency. *Liquid Penetrant and Magnetic Particle Testing at Level 2*; International Atomic Energy Agency (IAEA): Vienna, Austria, 2000.
23. Zolfaghari, A.; Zolfaghari, A.; Kolahan, F. Reliability and sensitivity of magnetic particle nondestructive testing in detecting the surface cracks of welded components. *Nondestruct. Test. Eval.* **2018**, *33*, 290–300. [CrossRef]
24. Payão Filho, J.D.C.; Passos, E.K.D.; Gonzaga, R.S.; Ferreira, R.F.; Santos, D.D.; Juliano, D.R. Ultrasonic Inspection of a 9% Ni Steel Joint Welded with Ni-based Superalloy 625: Simulation and Experimentation. *Metals* **2018**, *8*, 787. [CrossRef]
25. Berkache, A.; Lee, J.; Choe, E. Evaluation of Cracks on the Welding of Austenitic Stainless Steel Using Experimental and Numerical Techniques. *Appl. Sci.* **2021**, *11*, 2182. [CrossRef]
26. García-Martín, J.; Gómez-Gil, J.; Vázquez-Sánchez, E. Non-Destructive Techniques Based on Eddy Current Testing. *Sensors* **2011**, *11*, 2525–2565. [CrossRef]
27. Kim, J.; Le, M.; Lee, J.; Hwang, Y.H. Eddy current testing and evaluation of far-side corrosion around rivet in jet-engine of aging supersonic aircraft. *J. Nondestruct. Eval.* **2014**, *33*, 471–480. [CrossRef]
28. Li, C.; Liu, R.; Dai, S.; Zhang, N.; Wang, X. Vector-Based Eddy-Current Testing Method. *Appl. Sci.* **2018**, *8*, 2289. [CrossRef]
29. Spies, B.R. Depth of investigation in electromagnetic sounding methods. *Geophysics* **1989**, *54*, 872. [CrossRef]
30. AbdAlla, A.N.; Faraj, M.A.; Samsuri, F.; Rifai, D.; Ali, K.; Al-Douri, Y. Challenges in improving the performance of eddy current testing: Review. *Meas. Control* **2019**, *52*, 46–64. [CrossRef]
31. Rosado, L.S.; Janeiro, F.M. Defect characterization with eddy current testing using nonlinear-regression feature extraction and artificial neural networks. *IEEE Trans. Instrum. Meas.* **2013**, *62*, 1207–1214. [CrossRef]
32. Fan, M.B.; Cao, B.H.; Yang, P.P.; Li, W.; Tian, G.Y. Elimination of liftoff effect using a model-based method for eddy current characterization of a plate. *NDT E Int.* **2015**, *74*, 66–71. [CrossRef]
33. Xu, Z.; Wang, X.; Deng, Y. Rotating Focused Field Eddy-Current Sensing for Arbitrary Orientation Defects Detection in Carbon Steel. *Sensors* **2020**, *20*, 2345. [CrossRef]
34. Huang, L.; Liao, C.; Song, X.; Chen, T.; Zhang, X.; Deng, Z. Research on Detection Mechanism of Weld Defects of Carbon Steel Plate Based on Orthogonal Axial Eddy Current Probe. *Sensors* **2020**, *20*, 5515. [CrossRef] [PubMed]
35. Zhang, S.; Uchimoto, T.; Takagi, T.; Hashimoto, M.; Takeda, S. Mechanism study for directivity of TR probe when applying Eddy current testing to ferro-magnetic structural materials. *NDT E Int.* **2021**, *122*, 102464. [CrossRef]
36. Takagi, T.; Tani, G.; Fukutomi, H.; Hashimoto, M. Finite element modeling of eddy current testing of steam generator tube with crack and deposit. *Rev. Prog. QNDE* **1997**, *16*, 263–270.
37. ISO 9712*Non-Destructive Testing—Qualification and Certification of NDT Personnel*, 4th ed.; ISO: Geneva, Switzerland, 2012.
38. Kim, J.; Kim, S.; Le, M.; Lee, J.; Park, J. Detection and Evaluation of Backside Crack in Spot-welding Component of Heat-resistant Alloy Using Electromagnetic Field Distortion. *Int. J. Appl. Electromagn.* **2016**, *52*, 1193–1199. [CrossRef]
39. Silvester, P.; Chari, M.V.K. Finite element solution of saturable magnetic field problems. *IEEE Trans. Power Appar. Syst.* **1970**, *PAS-89*, 1642–1651. [CrossRef]
40. Ida, N.; Betzold, K.; Lord, W. Finite element modeling of absolute eddy current probe signals. *J. Nondestruct. Eval.* **1982**, *3*, 147–154. [CrossRef]
41. Oudni, Z.; Feliachi, M.; Mohellebi, H. Assessment of the probability of failure for EC nondestructive testing based on intrusive spectral stochastic finite element method. *Eur. Phys. J. Appl. Phys.* **2014**, *66*, 30904. [CrossRef]
42. Thomas, J.L. *Simplified Modeling of Eddy Current Control of Steam Generator Tubes*; Report of Internship, ESA IGELEC; University of Nantes: Nantes, France, 1998.

43. Takagi, T.; Hashimoto, M.; Fukutomi, H.; Kurohwa, M.; Miya, K.; Tsuboi, H.; Tanaka, M.; Tani, J.; Serizawa, T.; Harada, Y.; et al. Benchmark models of eddy current testing for steam generator tube: Experiment and numerical analysis. *Int. J. Appl. Electromagn. Mater.* **1994**, *5*, 149–162. [CrossRef]
44. Chen, D.; Shao, K.R.; Lavers, J.D. Very fast numerical analysis of benchmark models of eddy-current testing for steam generator tube. *IEEE Trans. Magn.* **2002**, *38*, 2355–2357. [CrossRef]